Remote Sensing of Environment 298 (2023) 113825

Contents lists available at ScienceDirect

Remote Sensing of Environment

journal homepage: www.elsevier.com/locate/rse

Modeling forest canopy surface retrievals using very high-resolution spaceborne stereogrammetry: (I) methods and comparisons with actual data

Tiangang Yin [a,b,c,d,*], Paul M. Montesano [b,e], Bruce D. Cook [b], Eric Chavanon [f], Christopher S. R. Neigh [b], David Shean [g], Dongju Peng [h], Nicolas Lauret [f], Ameni Mkaouar [b,i], Douglas C. Morton [b], Omar Regaieg [f], Zhijun Zhen [f], Jean-Philippe Gastellu-Etchegorry [f]

[a] Earth System Science Interdisciplinary Center, University of Maryland, College Park, MD 20740-3823, USA
[b] Biospheric Science Laboratory, NASA Goddard Space Flight Center, Greenbelt, MD, USA
[c] Department of Land Surveying and Geo-Informatics, The Hong Kong Polytechnic University, Hung Hom, Hong Kong
[d] JC STEM Lab of Earth Observations, Department of Land Surveying and Geo-Informatics, The Hong Kong Polytechnic University, Hung Hom, Hong Kong
[e] Science Systems and Applications, Inc., Lanham, MD, USA
[f] Centre d'Etudes Spatiales de la Biosphère – UT3, CNES, CNRS, IRD, Université de Toulouse, 31401 Toulouse Cedex 9, France
[g] Department of Civil and Environmental Engineering, University of Washington, Seattle, WA, United States
[h] Earth Observatory of Singapore, Nanyang Technological University, Singapore
[i] Goddard Earth Sciences and Technology Research II, University of Maryland Baltimore County, Baltimore, MD, 21250, USA

ARTICLE INFO

Keywords:
Radiative transfer model
Photogrammetry
Stereogrammetry
Surface elevation
Canopy structure
Open forest
Closed forest
Worldview
LiDAR
NASA STV
Solar zenith angle
Convergence angle
Camera model

ABSTRACT

The capability of spaceborne stereogrammetry using very high-resolution (VHR, <2 m) imagery with various environmental, experimental, and sensor configurations for characterizing forest canopy surfaces has not been completely explored. Existing archives of VHR imagery include a limited subset of potential stereo image acquisition configurations and may therefore exclude optimal configurations for capturing critical structural features of forest canopy surface. By contrast, simulated VHR imagery from 3-D radiative transfer models (RTM) can explore the full range of spatial, spectral, and sun-sensor configurations to identify factors that contribute to uncertainties in stereo-derived estimates of forest canopy structure. We developed a novel method to simulate VHR stereopairs using the discrete anisotropic radiative transfer (DART) model and then derive surface elevations from the simulated images. We reconstructed one open-canopy and one closed-canopy forest scene and created a reference digital surface model/digital terrain model (DSM/DTM) using airborne small-footprint lidar points over the study sites. The VHR simulations were configured to match three independent WorldView stereopairs. The results showed that, compared to the reference DSM, the surface elevations derived using simulated and WorldView image data were consistent, with differences of <1.6 m in vertical bias, < 1 m in root mean square error (RMSE), and < 0.07 in correlation coefficient (R). We demonstrated that realistic 3-D RTM simulations could be georeferenced with a camera model for DSM generation from simulated stereopairs. This work will support a follow-up investigation that examines stereo-derived DSM quality over a broad range of surface types and acquisition parameters to suggest optimal configurations for actual VHR stereo data acquisition of vegetation canopy surfaces.

1. Introduction

Forests cover 31% of the Earth's land surface and contribute important ecosystem services, such as biodiversity conservation and carbon sequestration (Aber et al., 1996; Mitchard, 2018). Canopy structure is a fundamental attribute of forested ecosystems. Variations in canopy structure reflect differences in forest type and forest disturbances ranging from tree fall gaps (Antonarakis et al., 2014) to large-scale impacts from natural hazards (Feng et al., 2020; Parker et al., 2018) and human activities (Asner et al., 2004; d'Oliveira et al., 2021). Remote

* Corresponding author at: Earth System Science Interdisciplinary Center, University of Maryland, College Park, MD 20740-3823, USA.
E-mail address: tiangang.yin@polyu.edu.hk (T. Yin).

https://doi.org/10.1016/j.rse.2023.113825
Received 2 June 2022; Received in revised form 3 September 2023; Accepted 17 September 2023
Available online 25 September 2023

sensing by Earth observation satellites is the most efficient way to monitor global forest cover and characterize canopy structure (Jones and Vaughan, 2010). In recent years, there has been rapid growth in the availability of spaceborne acquisitions of very high-resolution (VHR) images (<2 m spatial resolution) (Lesiv et al., 2018). The use of 3-D stereogrammetric reconstruction from VHR images can provide large-scale information regarding surface elevations (Abrams et al., 2020; Neigh et al., 2014, 2016; Noh and Howat, 2017; Shean et al., 2016; St-Onge et al., 2008; Tadono et al., 2014). However, compared to the relatively mature elevation and height estimates of urban infrastructure (Dissegna et al., 2019; Qin, 2014; Tack et al., 2012) and snow/ice surfaces (Howat et al., 2019; Porter et al., 2018; Shean et al., 2020), the capability and accuracy of VHR stereogrammetry to derive forest canopy surfaces has received relatively limited attention (Montesano et al., 2019; Piermattei et al., 2018).

The reliability of stereo-reconstructed surfaces relies on the density and accuracy of point locations to extract parallax, derived from the correlations among matched textures identified from different view directions. Non-Lambertian surfaces can greatly complicate stereo texture matching to derive stereo products (Shi et al., 2016; Sun et al., 2007). Vegetation is a non-Lambertian surface type, due in part to the influence of leaf clusters and branches with a strong anisotropic bidirectional reflectance factor (BRF) distribution as a result of incident solar radiation and view direction (Roujean et al., 1992; Schaepman-Strub et al., 2006; Wu et al., 2019). For images acquired from VHR sensors, the region covered by each pixel has its own unique structural (e.g., crown shape, clumping, vegetation cover fraction), biophysical (e.g., leaf area index, leaf angle distribution), and foliar biochemical (e.g., pigments) properties. These properties vary among different species and locations within a tree crown. Therefore, the image texture varies in a complex way due to the changing canopy reflectance of the matched pixels over a given forest observed from different view directions.

Understanding the accuracy of stereo-reconstructed forest canopy surfaces requires 1) a statistically significant number of multi-view VHR images; 2) an ideal test site with high-fidelity canopy surface and terrain references derived from airborne or field measurements. For the latter, frequent airborne laser scanning (ALS) acquisitions, such as the National Ecological Observatory Network (NEON, Kampe et al., 2010) and NASA Goddard's LiDAR, Hyperspectral & Thermal (G-LiHT, Cook et al., 2013) Airborne Imager provide open-access references, including the products of the high-resolution digital surface models (DSMs), digital terrain models (DTMs), and canopy height models (CHMs, here defined as $DSM - DTM$) over several forest sites. However, access to a large amount of spaceborne data from VHR platforms over a selected forest study site is limited. In addition, many existing VHR stereo datasets were collected with standard configurations (e.g., $\sim 35^{\circ}$ convergence angle for along-track stereopairs by WorldView to balance the accuracy and occlusion for most Earth surface targets, rather than forests), limiting the ability to study the range of configurations that influence the accuracy of stereo-derived forest height and structure. Although cross-track stereo combinations (imagery collected on subsequent orbits/days) could fill certain gaps in the range of sensor configurations from along-track data collection, differences in sun-sensor geometry, atmospheric conditions, and environmental factors on the terrain would increase the uncertainty of the results (Qin, 2019).

Simulated data can be used to compensate for the lack of observational data. For example, the LandStereo model (Ni et al., 2019a, 2019b) has been developed to simulate stereopairs for surface reconstruction. However, the bidirectional reflectance distribution function (BRDF) properties of the terrain and vegetation were not considered, and the description of the forest landscape was not realistic compared with the actual data. In contrast, physical-based radiative transfer models (RTM) have the potential to accurately simulate high-resolution remote sensing measurements over forests across the full range of instrumental, experimental, and environmental configurations (Myneni et al., 1992). Among the existing RTMs, 3-D ray tracing based RTMs are suitable for exploring the influence of complex forest structures on VHR images based on their ability to simulate realistic 3-D mock-ups and model radiation interactions with reduced simplifications and assumptions (Disney et al., 2000; Gastellu-Etchegorry et al., 2015; Goodenough and Brown, 2012; Govaerts and Verstraete, 1998; Kobayashi and Iwabuchi, 2008; North, 1996; Qi et al., 2019; Zhao et al., 2022). Most importantly, for each ray that enters the sensor, the ray-tracing approach connects the scene coordinates where the ray originated, to the projected image pixel index, which provides information of control points for building various sensor acquisition geometries (Chai and Shum, 2000; Gupta and Hartley, 1997; Sonka et al., 2014).

The discrete anisotropic radiative transfer (DART) model (Gastellu-Etchegorry et al., 1996, 2015) is a 3-D ray tracing RTM that can be enhanced to simulate VHR stereopairs for deriving the canopy surface information. DART has been characterized as part of the radiative transfer intercomparison (RAMI) benchmark evaluations and accurately models the BRF of homogenous and heterogeneous vegetation (Widlowski et al., 2007). Sensor perspective projection was implemented in DART (Yin et al., 2015) to expand the model flexibility for image simulation, including the spatial resolution, number of bands, and view directions (Yin et al., 2013). The latest release of the DARTDAO (data access object) built-in tool (DART, 2023) facilitates scene creation using voxels of 3-D leaf area density (LAD) derived from airborne and terrestrial lidar data (Kükenbrink et al., 2021; Regaieg et al., 2021; Wei et al., 2020). DART-simulated images using lidar-derived scenes can be comparable to a broad range of actual VHR images based on the radiance value of each pixel (Qi et al., 2018; Schneider et al., 2014a, 2014b). These comparisons could be further extended to image processing and computer vision products derived from VHR images, such as DSM reconstruction from stereopairs using existing software packages.

In this study, we developed a novel method to simulate VHR stereopairs for DSM reconstruction using DART, aiming to study the capacity and accuracy of forest surface retrieval using more flexible instrumental and experimental configurations than what is currently available from existing satellites. We compared DSMs derived from DART-simulated and observed (WorldView) VHR stereo images over two forested sites, one representing closed and one representing open-canopy conditions. Therefore, this work outlines the steps to simulate VHR stereopairs using DART and evaluate model simulations against observations and reference data. Together, these advances form the basis of the model development required to provide a tool to support further study of optimal imaging configurations for stereogrammetry over complex forest vegetation (Yin et al., 2023).

2. Study sites

We chose two study sites (Fig. 1) to investigate two general forest types, whose canopy surfaces cover a range of textures and structural patterns. The first is a 36 ha closed-canopy forest at the Smithsonian Environmental Research Center (SERC), a ForestGEO site[1] in Edgewater, MD, USA. The second is a 16 ha open-canopy forest with a heterogeneous cover at the Gus Pearson Natural Area[2] (GPNA) in Flagstaff, AZ, USA. Multi-path G-LiHT airborne lidar campaigns were conducted over both sites, resulting in lidar point densities of $\sim 51/m^2$ for SERC (28 June 2012), and $\sim 22/m^2$ for GPNA (31 March 2013). We cropped the G-LiHT point clouds (red squares in Fig. 1) for each study site to generate DART model scenes for image simulations.

The SERC site is located approximately 50 km east of Washington, DC, the Eastern USA. The mixed-species deciduous forest is dominated by *Liquidambar styraciflua* (sweetgum) and *Liriodendron tulipifera* (tulip poplar) in the overstory, and *Carya tomentosa* (hickory), *Quercus alba* (white oak), and *Fagus grandifolia* (beech) in the understory (Kamoske

[1] https://forestgeo.si.edu/sites/north-america/smithsonian-environmental-research-center

[2] https://www.ser-rrc.org/project/usa-arizona-gus-pearson-natural-area-restoration/

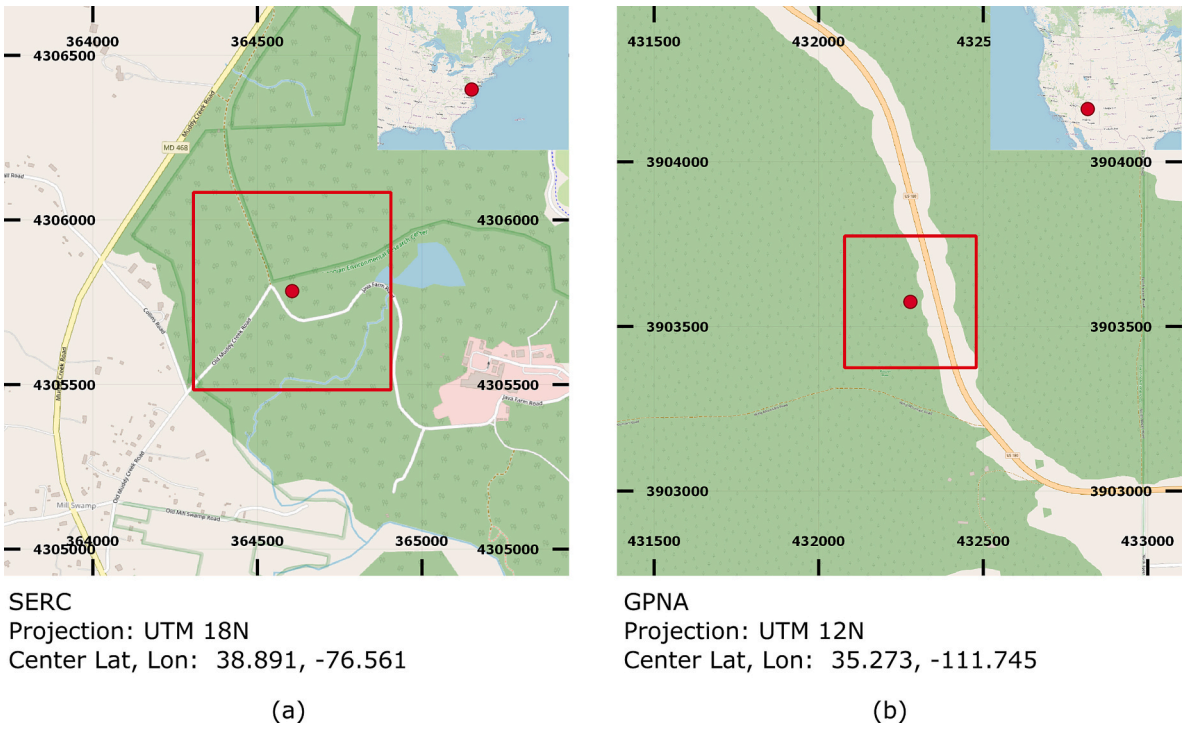

Fig. 1. Study site locations. (a) Smithsonian Environmental Research Center (SERC) in Edgewater, MD, USA, and (b) Gus Pearson Natural Area Forest (GPNA) in Flagstaff, AZ, USA. Red squares indicate the extent of each simulated forest scene: (a, $600 \times 600 m^2$, Projection: UTM 18 N) and (b, GPNA, AZ, Area: $400 \times 400 m^2$, Projection: UTM 12 N). (For interpretation of the references to colour in this figure legend, the reader is referred to the web version of this article.)

et al., 2019; Parker, 1995). High vegetation fractional cover (reaching 97%) reflects mature (~125 years) and intermediate (~75 years) second-growth forests at the site. The DSM, DTM, and CHM at 1 m resolution derived from G-LiHT lidar acquisitions are shown in Fig. 2a. The DSM was derived from the 1st returns of the lidar point cloud, and the DTM was derived from ground returns identified using a progressive morphological filtering method (Zhang et al., 2003). The CHM was generated by subtracting the DTM from the DSM. For SERC, the majority (20—100 percentile) of the canopy height was above 25 m, forming a normal distribution centered at the height of 31 m in the histogram.

In contrast, the GPNA site (12 km northwest of Flagstaff, AZ, the Southwestern USA) represents an open forest (~50% vegetation fractional cover) of evergreen *Pinus ponderosa*. The heterogeneous cover at the GPNA partly reflects a thinning treatment applied between 2006 and 2007 to reduce fuel accumulation that could trigger a hazardous fire (Flathers et al., 2016; Wallin et al., 2004). Since then, no intervention has been applied at the selected site (Duncanson et al., 2015). As shown in Fig. 2b, the majority of the CHM distribution (0—80 percentile) is below 18 m, forming a normal distribution centered at the height of 10 m. The heights of trees in the 80—100 percentiles can reach >35 m (3 times the median height), and these old pines have well-developed crowns visible in the reference CHM. It should be noted that even the tallest trees had crown diameters of only 5—10 m. These tall, slender trees are challenging for stereo reconstruction because of the enhanced structural variation from different view directions.

The DSM and DTM in Fig. 2 were used as references (DSM_{ref} and DTM_{ref}) for evaluation of surface elevation retrievals from simulated and observed VHR stereopairs. Both SERC and GPNA have relatively flat terrains, with mean slopes < 5° across each study area.

3. Methods

3.1. Biophysically realistic construction of 3-D model scenes using G-LiHT airborne lidar data

The PVlad model (Yin et al., 2022) was applied to the multi-path lidar data of G-LiHT to reconstruct the simulated scenes using a 0.5 m voxel dimension for DART simulations. PVlad is a physical-based method that reduces the need for associated field measurements (Yin et al., 2020) in 3-D plant area density (PAD) estimation from airborne lidar. Yin et al. (2022) constructed eight mature, logged, and intermediate-aged stands of a 1-ha area over SERC (areas embedded within the current study site) from PVlad using leaf-on and leaf-off G-LiHT data. Validation results showed robust estimations for 0.5 m voxel dimension with RMSE <0.60 m^2/m^2 for overall leaf area index compared with direct litter-collection measurements, and a strong correlation was observed with $R \approx 0.9$, and RMSE <0.03 m^2/m^3 for leaf area density vertical distribution compared with independent terrestrial lidar field-survey measurements conducted by Béland and Baldocchi (2021). For this work, PVlad was applied over a much larger area over SERC and GPNA with 3-D PAD voxels and 2-D PAI pixels, as shown in Fig. 3. The overall derived PAI was 5.23 m^2/m^2 and 1.78 m^2/m^2 for SERC and GPNA, respectively. It can be observed that the crowns with the highest PAI are almost evenly distributed in the dense forest of SERC, and they correspond to the old pines in GPNA, correlated with the 80—100 CHM percentile in Fig. 2. The effective leaf dimension was set to 0.1 cm^2 to simulate the hotspot effect of leaf clusters following Myneni and Ross (2012).

3.2. Simulation of stereogrammetry

Fig. 4 illustrates the three-path workflow to generate DSMs or DTMs from the G-LiHT lidar data or from the simulated and WorldView VHR stereopairs. Evaluations and comparisons of the derived DSMs from all three approaches consider the same study area extent.

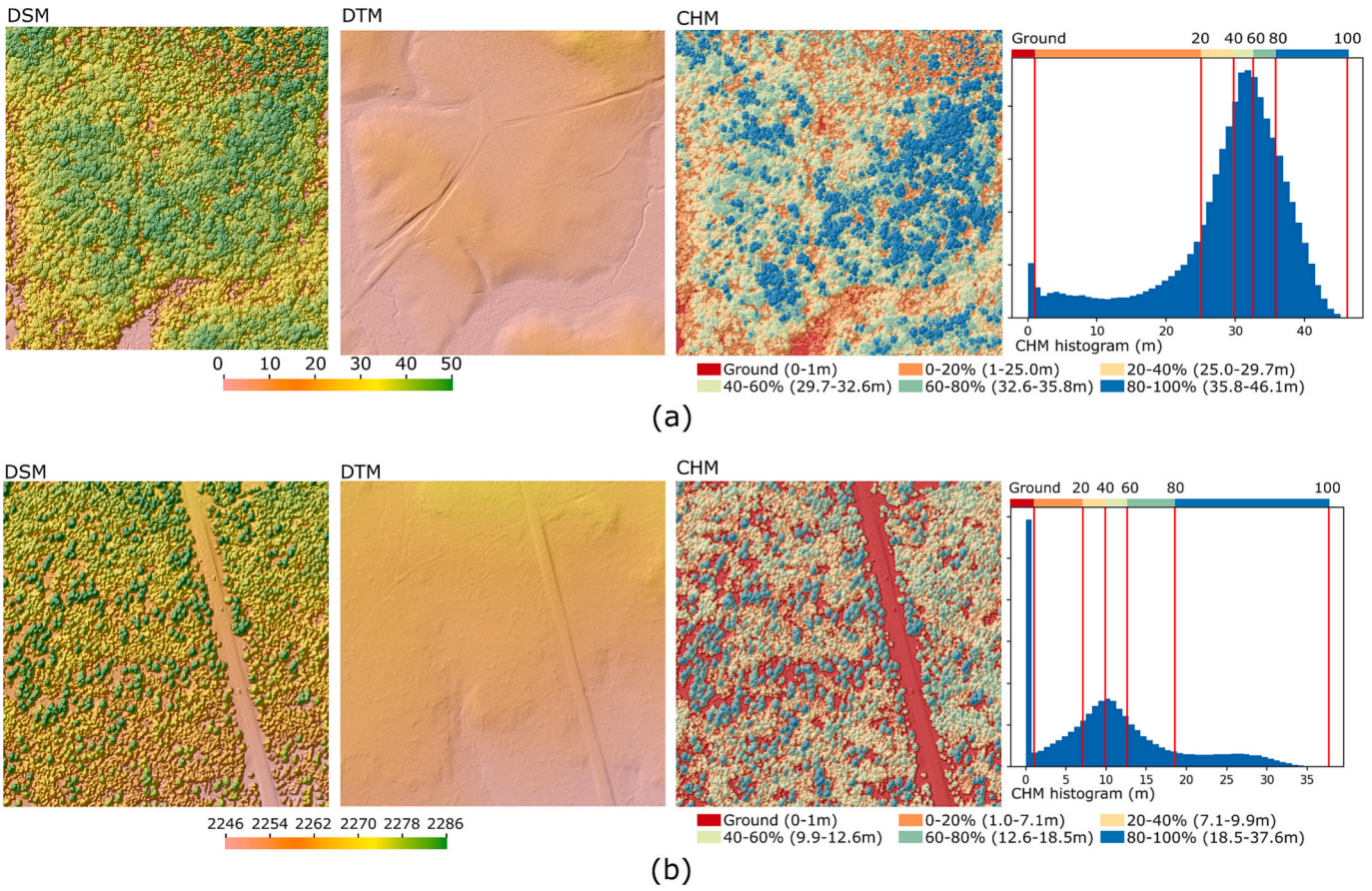

Fig. 2. High-fidelity reference data derived from G-LiHT point clouds over the study sites, including the 1 m resolution DSM, DTM, and CHM percentile distribution and histograms over (a) SERC and (b) GPNA (see Fig. 1 for context). Elevation values are orthometric heights above the Earth Gravitational Model EGM96 geoid vertical datum (Lemoine et al., 1998).

3.2.1. *DART imagery simulation background*

DART is an Earth-atmosphere coupling model validated against MODTRAN in the top of atmosphere (TOA) radiance from the visible to the thermal infrared spectral domains (Grau and Gastellu-Etchegorry, 2013; Morrison et al., 2020; Wang and Gastellu-Etchegorry, 2021). In DART, incoming solar radiation is traced among the TOA, the top of the canopy (TOC), and the Earth scene. The direct and diffuse atmospheric irradiance were computed over the TOC, which determined the SKYL (percentage of diffuse irradiance to the total irradiance) at the TOC. SKYL is a key parameter for determining the depth of shadow textures generated by leaves, canopy shape, and vegetation fractional cover, which are critical features captured by stereogrammetry.

Over the Earth scene, DART simulates heterogeneous landscapes composed of 3-D voxels as the storage of the Earth's vegetation structural, air and surface elements, and the intercepted radiation. The two basic ways to represent the elements within each voxel are the 2-D facets (leaves, topography, building, etc.) and 3-D turbid cells (leaf cluster, air, fluids, etc.). Radiation attenuation and interception within turbid cells follow Beer's law. The scattering of intercepted radiation follows the precomputed transfer function derived from a number of discrete angular sectors. Ray tracing was performed until convergence was achieved after several iterations. Image acquisition varies among different types of camera models and sensor platforms (Chai and Shum, 2000; Gupta and Hartley, 1997; Sonka et al., 2014), such as the parallel projection for infinite-distance sensors, the perspective projection for frame cameras, and the parallel-perspective projection for linear pushbroom imagers (parallel projection along the track direction and perspective projection along the cross-track direction). To account for these configurations in the simulation, for each scattering event, a ray is sent towards the sensor according to the acquisition geometry and solid angle, and finally intercepted by an image plane (Yin et al., 2015). These intercepted rays accumulate and convert into radiance per pixel to generate sensor imagery.

3.2.2. *Rational Polynomial Coefficients (RPC) model implementation*

In most VHR imagery acquisitions, the platforms are typically modeled by building the projection of the 2-D image pixel index (l, s) to 3-D geocoordinates (lat, long, height) described with 78 RPCs (Fraser and Hanley, 2003) using a list of ground control points (GCPs) (Tao and Hu, 2001). To derive these GCPs, the 3-D Cartesian system of the Universal Transverse Mercator (UTM) bridged the interconversion between geocoordinates (lat, long, height) and DART scene local coordinates (x, y, z), which constructed the initial georeferencing and projection of the DART simulated images. During ray tracing, each ray that enters the sensor generates a correspondence projection from its starting position (x, y, z) onto the 2-D image pixel index (l, s). Therefore, using UTM interconversion, the geocoordinates (lat, long, height) can be mapped with (l, s). Such information of randomly selected 500–1000 rays across the scene was extracted as a novel product of DART associated with each simulated image. The created GCP list of $(lat, long, height) \rightarrow (l, s)$ is used to solve the RPCs using nonlinear least-squares estimation. Following an initial estimate from least squares using the linear part of the RPC transform, the Levenberg–Marquardt algorithm is used through an efficient iterative process until the convergence of accuracy is achieved to precisely determine RPCs (Fletcher, 1971; Moré, 1978). Hereafter, the initially simulated images of DART in the ILWIS format are converted into GeoTIFF format, with the scene boundaries and RPCs stored in the metadata. Based on high-fidelity scenes derived from PVlad, the

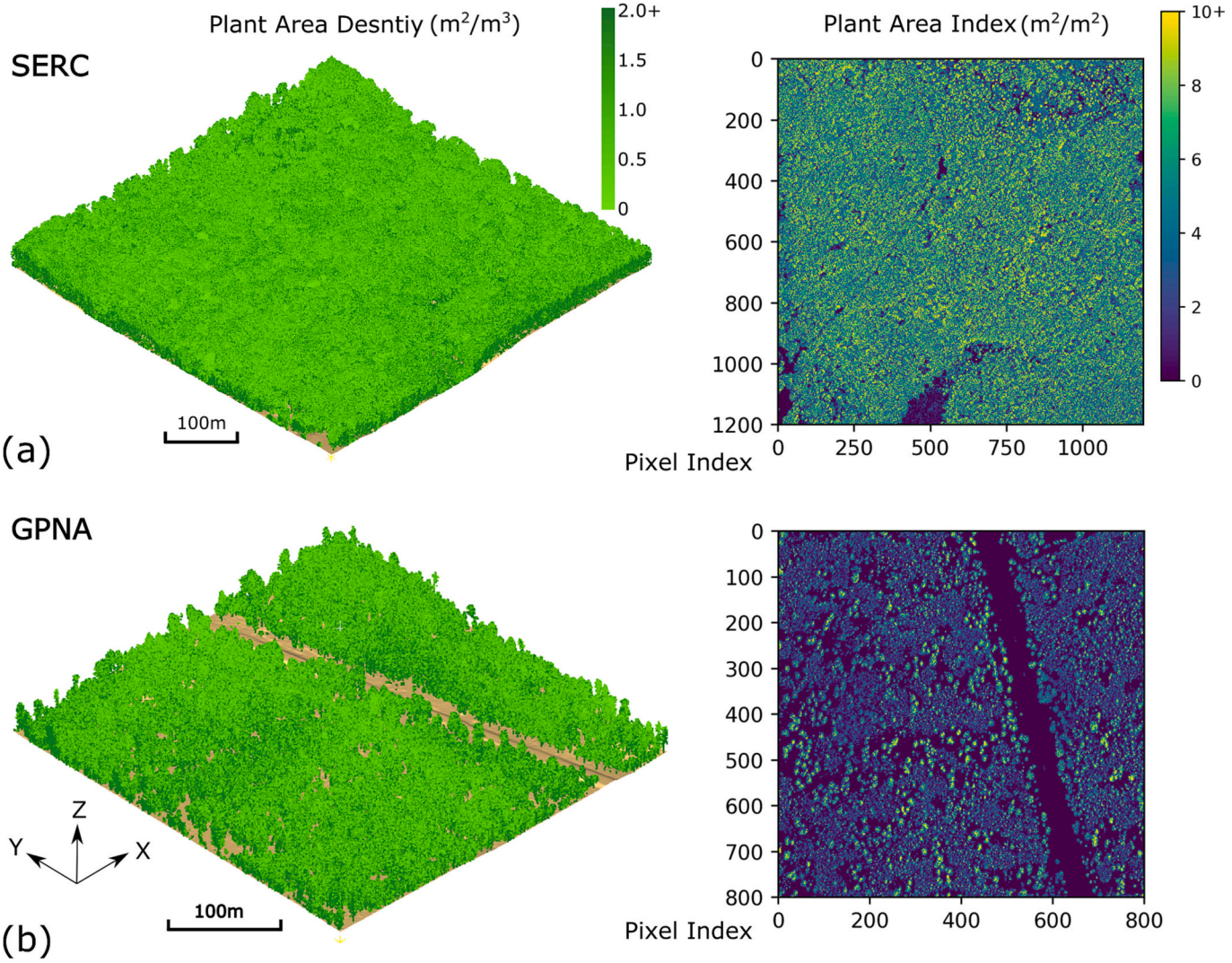

Fig. 3. The 3-D scene for the (a) SERC and (b) GPNA sites created using the lidar-derived PAD per voxel, and the corresponding maps of PAI of 0.5 m voxel dimension.

simulated images could be precisely registered with actual remote sensing data using the same acquisition geometry, facilitating the validation and improving the universal compatibility for post-processing using existing image data processing software.

3.2.3. DSM generation from simulated stereopairs

We used the NASA Ames Stereo Pipeline (ASP, Beyer et al., 2018; Moratto et al., 2010; Shean et al., 2016) to generate DSMs from each set of DART-simulated stereopairs. The software configurations followed the same settings as the workflow of mass-processing VHR images in the NASA Center for Climate Simulation's Advanced Data Analytics Platform (ADAPT) (Montesano et al., 2017, 2019). The scene boundaries, coordinate systems, and geolocation accuracy were consistent between the DART-simulated stereopairs and lidar reference. The stereo correlation algorithm employs an iterative semi-global matching method and an affine-epipolar alignment approach for tie-point detection (d'Angelo and Reinartz, 2012; Hirschmuller, 2008; Rothermel et al., 2012; Xiang et al., 2016). The cost function during correlation used the ternary census transform associated with the semi-global matching (SGM) (Hu et al., 2016). The correspondences between the pixels of the input images used a kernel of 7 × 7 pixels to match the features through a cross-correlation algorithm applied to regionally normalized pixel values. Subpixel refinement applied the Bayes expectation-maximization correlator using an affine adaptive window within each kernel (Nefian et al., 2009). Triangulation was performed using the RPC models to generate dense point clouds without filtering or eroding. We used the ASP point2dem utility to generate DSMs with a 1 m ground sample distance (GSD).

3.3. Comparison between simulation and WorldView data

3.3.1. Simulation configurations

The simulation results were compared to three cloud-free WorldView along-track panchromatic stereopairs as shown in Table 1 (acquisitions named View1 and View2 for each pair; one pair over SERC and two pairs over GPNA represented as GPNA1 and GPNA2). Maxar provides Level-1B images to federal government agencies and non-profit organizations through the NextView license agreement (Neigh et al., 2013) (https://cad4nasa.gsfc.nasa.gov/). The WorldView acquisition date over SERC was close to the G-LiHT campaign date, whereas those over GPNA were approximately seven years after the G-LiHT campaign because of the lack of data coverage. Nevertheless, the evergreen forests of pine have not been changed due to logging or hazard. The limited data showed that the lack of statistically significant datasets over the same study site for the sensitivity study was the major constraint of actual data and the primary reason for using simulated data. The GSD ranged from 0.52 to 0.68 m for SERC (WorldView-1) and from 0.34 to 0.41 m for

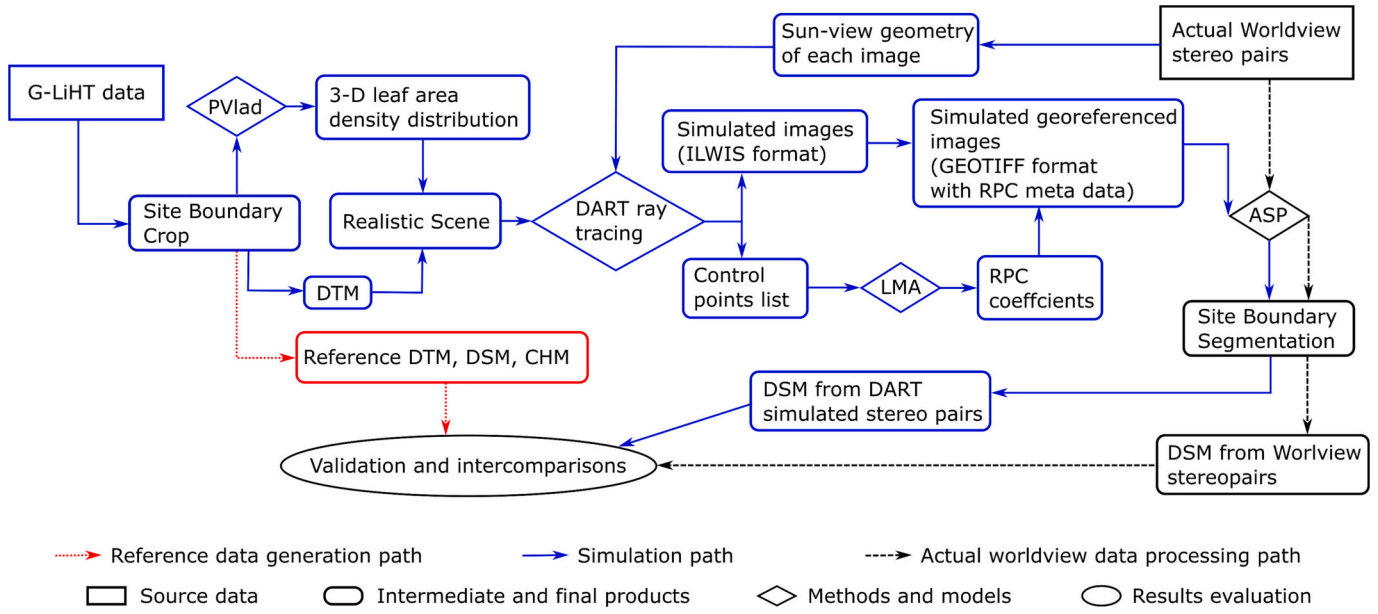

Fig. 4. The workflow of stereopair simulation and evaluation in three separate paths, including 1) generating reference data (dotted path); 2) processing simulation (solid path); 3) processing WorldView data (dashed path). ILWIS: Integrated Land and Water Information System; RPC: Rational Polynomial Coefficients; ASP: Ames Stereo Pipeline; LMA: Levenberg–Marquardt Algorithm.

Table 1
Three selected WorldView stereopairs over SERC and GPNA for comparison with reference and simulation.

Site / Platform	SERC / WorldView-1		GPNA1 / WorldView-3		GPNA2 / WorldView-3	
Date	2012-06-15		2020-04-26		2020-05-01	
Solar Zenith (°)	19.21		23.91		24.82	
Solar Azimuth (°)	140.71		150.74		139.11	
Convergence Angle (°)	36.99		35.07		44.00	
Acquisitions	View1	View2	View1	View2	View1	View2
GSD (m)	0.52	0.68	0.34	0.40	0.34	0.41
View Zenith (°)	12.96	35.50	23.96	33.81	26.63	35.72
View Azimuth (°)	299.37	211.74	303.84	229.03	65.06	156.48

GPNA (WorldView-3). For each along-track stereopair, the difference between the solar directions for the two views is negligible. The convergence angle between the two view vectors ranged from 35.07° to 44.00° (within the standard stereo acquisition range used by Maxar).

For the reconstructed forest scenes over SERC and GPNA, the topography is represented by facets that are triangulated using ground returns of ALS, and the trees are represented by turbid cells in terms of 3-D distributions of PAD, which are computed by the PVlad model. The DART simulations followed the same sun/view direction configurations as the corresponding WorldView acquisitions. Panchromatic stereopairs of each scene were simulated by DART using a general foliar reflectivity of 0.263 and a Lambertian ground reflectivity of 0.097, derived from the default DART reflectance spectrum database of "deciduous leaf" and "plantation soil". These generic format properties are suitable for the broad spectral domain (450–800 nm), which approximates the WorldView panchromatic band. The TOA images were simulated by coupling a clear-sky atmosphere using the USSTD76 gas model and the RURAL aerosol (visibility of 23 km) model (Berk et al., 1987; Gastellu-Etchegorry et al., 2017). The default GSD of the simulated images was set to 0.5 m—the same as the voxel dimension. However, the spatial resolution could be larger than 0.5 m owing to the approximated cubic voxel shape spanning over different pixels after projection along the view direction, and the point spread function of the WorldView instruments. Due to the small simulated scene size ($600 \times 600 m^2$) and the ~400-617 km altitude of the Worldview satellites, the directional variation (angle of view) across the whole scene is <0.05 degrees, which can be neglected. A horizontal image plane was used to intercept the rays for image generation, as described in Yin et al. (2015). The generated RPC describes the coordinate-pixel mapping of the GCPs for the simulated raw images.

3.3.2. Evaluation metrics

After running ASP with identical processing settings for both WorldView and simulated VHR stereopairs, DSMs of 1 m GSD were generated ($DSM_{gen,WV}$ and $DSM_{gen,sim}$, respectively) to facilitate comparison with the reference DSM and DTM derived from G-LiHT data (DSM_{ref} and DTM_{ref}). Indeed, the scenes constructed based on a G-LiHT dataset had exact correspondences of coordinates as the DTM_{ref} and DSM_{ref}, which were also derived from the same dataset without any geolocation bias. Relying on the matched texture (canopy, terrain, etc.) identified from different views, the stereo-derived DSM exhibits feature losses compared to the references. For example, if only terrain textures were identified and all vegetation textures were missed, the DSM_{gen} would be close to DTM_{ref} instead of DSM_{ref}.

It is essential to estimate the shift compared to DTM_{ref} or DSM_{ref}, and then to co-register the generated DSM to the references ($DSM_{gen} \rightarrow DSM_{cr}$) to evaluate local accuracy. The co-registered DSM derived from both WorldView and simulations ($DSM_{cr,WV}$ and $DSM_{cr,sim}$) can be achieved using the point cloud alignment approach implemented in ASP based on the libpointMatcher library (Pomerleau et al., 2013). To evaluate the comparisons with the references, we deployed two variables that were used by Montesano et al. (2017): 1) bias of vertical co-registration against the references ($Bias_z$), and 2) accuracy ($RMSE'$) of co-registered DSM (DSM_{cr}) features against the references. $Bias_z$ can be computed as:

$$Bias_z = mean\left(DSM_{gen}\right) - mean\left(DTM_{ref} \text{ or } DSM_{ref}\right) \quad (1)$$

$Bias_z$ (typically systematic) indicates the absolute height offset. After co-registration, we computed the accuracy as the root mean square error of all pixels ($RMSE'$, with $'$ notation indicating values for the co-registered DSM_{cr} against the references), which is critical for evaluating whether DSM_{cr} captured the actual feature of surface variation compared with the references:

$$RMSE' = RMSE\left(DSM_{cr}, DTM_{ref} \text{ or } DSM_{ref}\right) \quad (2)$$

4. Results

4.1. Comparisons of DSMs

4.1.1. Comparisons of DSMs derived from the simulations and WorldView data against the references

Fig. 5 illustrates detailed comparisons of SERC, GPNA1, and GPNA2 between 1) WorldView and simulated stereopairs at TOA (the 1st and 2nd columns); 2) the derived DSMs (the 3rd column); 3) correlation of the derived DSMs to DTM_{ref} and DSM_{ref} (the 4th column).

The WorldView and simulated TOA images radiometrically differed in certain localized regions due to the imperfection of simulation as observed from the 1st and 2nd columns of Fig. 5, although accurately derived 3-D structures of the forest were used. For example, comparing the 1st and 2nd rows of SERC in Fig. 5a shows that radiance variations among different tree species due to foliar biochemical content (e.g., pigments, water content, etc.) were not simulated; for GPNA (Fig. 5 bc), a homogenous ground property was used, so the contrast between the crown and the background in simulated images can be different from reality. However, these discrepancies did not hamper the use of simulated images to generate realistic DSM products using the panchromatic band because the key textures induced from the more predominant configurations of DSM retrieval, the sun-sensor geometry, were identified. The simulation from different views captured the directional variations of textures in terms of the top canopy structure over dense forests (SERC) and the geo-optical relationship between crowns and shadows of individual trees over open forests (GPNA). For example, the shadows were less visible in View2 of GPNA2 (Fig. 5c) because of the influence of the sun direction and View2 direction are close to each other (hotspot effect) in both WorldView and simulated images.

The DSMs were reconstructed similarly from WorldView and simulated stereopairs, so that both their results can be compared against the references. The 3rd column of Fig. 5 shows the $DSM_{gen,WV}$ and $DSM_{gen,sim}$ derived from the WorldView data and simulations. The DSMs used the same colormap and scale as DTM_{ref} and DSM_{ref} shown in Fig. 2. The $DSM_{gen,WV}$ were cropped from the DSM product of a strip of ~10 km swath, so the entire study sites were covered. In contrast, the $DSM_{gen,sim}$ used the simulated stereopairs prepared for the small site areas, so areas near the resulting DSM margins have artifacts and/or missing values. Also, taking G-LiHT lidar data as the reference neglected the canopy growth of evergreen forests for seven years over GPNA until the WorldView acquisitions. In addition, the geolocation error of WorldView, which could cause a vertical offset to the generated DSM, was not simulated. The RPC inaccuracy could also exist in WorldView data. Theoretically, the simulated RPCs should be more accurate than the WorldView RPCs derived for a much larger area. Within the small simulated scene ($600 \times 600m^2$), the results of RPC inaccuracy can be approximated by minor affine transformation, which can be corrected in $DSM_{gen,WV}$ by the co-registration.

Visually, the DSM_{gen} inter-comparisons indicated a relative consistency between the WorldView and simulation, except that the simulation results had a few sharper features. This could be caused by the well-defined groups of cubic voxels with 0.5 m size that constructed the 3-D scenes. In this context, the simulation using cubes could generate subtle subpixel textures from cube facets and vertices that do not exist in the real world. Initial visual comparisons with the high-fidelity references (Fig. 2) demonstrated consistency between $DSM_{gen,WV}$ and $DSM_{gen,sim}$: For SERC, both captured the elevation of the top canopy structure but became smoother by missing sharp features from DSM_{ref}. For GPNA1, both missed the major features from DSM_{ref}, especially for the structure of protruding old pines, so an intermediate elevation between DTM_{ref} and DSM_{ref} was obtained. For GPNA2, more crown features were missed owing to the hotspot effect that caused considerable texture variability in the crown reflectance and the reduced shadows of crowns on the ground in View2. Both $DSM_{gen,WV}$ and $DSM_{gen,sim}$ of GPNA2 were closer to DTM_{ref} than DSM_{ref}.

The observations of visual comparison were confirmed by the correlation of each DSM_{gen} against their corresponding references (red dots for DSM_{ref} and blue dots for DTM_{ref}), which are plotted in the 4th column of Fig. 5. For each correlation, we computed $Bias_z$ [Eq. (1)], the $RMSE'$ [Eq. (2)], and the correlation coefficient (R), to quantitatively evaluate the results. For SERC, a small $Bias_z$ against DSM_{ref} (0.21 and 1.72 m) and a large $Bias_z$ against DTM_{ref} (31.34 and 32.84 m) were observed for both WorldView and simulations, associated with a larger $RMSE'$ against DSM_{ref} (6.64 and 6.30 m) than DTM_{ref} (3.26 and 3.61 m). This was caused by the strong smearing effect of sharp features in the DSM_{cr} compared to the high fidelity DSM_{ref}, whereas DTM_{ref} was relatively smooth and therefore had better matching textures after co-registration. For GPNA1, both WorldView and simulations generated a negative $Bias_z$ against DSM_{ref} (−6.95 and − 5.99 m) and a positive $Bias_z$ against DTM_{ref} (3.44 and 4.40). The $RMSE'$ were similar against DSM_{ref} (8.59 and 9.31 m), whereas simulations had a higher $RMSE'$ against DTM_{ref} (4.45 m) than WorldView (2.22 m), owing to the sharper features of the generated DSM from simulations. For GPNA2, both $DSM_{gen,WV}$ and $DSM_{gen,sim}$ were closer to DTM_{ref} than DSM_{ref}, which was confirmed by a large negative $Bias_z$ towards DSM_{ref} (−8.01 and − 9.42 m) and a small positive $Bias_z$ towards DSM_{ref} (2.35 and 0.93 m). The $RMSE'$ against DSM_{ref} (8.40 and 8.61 m) was much larger than that against DTM_{ref} (0.48 and 1.61 m). The correlations with DTM_{ref} also showed a considerably strong $R > 0.94$.

4.1.2. Intercomparisons of DSMs derived from the simulations and WorldView data

Intercomparison between $DSM_{gen,WV}$ against $DSM_{gen,sim}$ revealed the spatial distributions of the differences (Fig. 6). For SERC, the differences were relatively consistent, except for the boundaries. At the lower edge, where the dense canopy transits to a flat region, $DSM_{gen,sim} < DSM_{gen,WV}$ indicated that less smearing effect was obtained for the DSM derived from simulated data. At the top-right corner, where the dense canopy is converting to a partially open canopy as shown in Fig. 1, $DSM_{gen,sim} > DSM_{gen,WV}$ indicated that the simulated images had more matched textures from the open canopy. This effect was also observed for GPNA1, $DSM_{gen,sim} > DSM_{gen,WV}$ for the lower canopy (younger pines) where slightly more textures were captured from the simulated data. However, it is interesting that DSMs generated from both WorldView and simulated images cannot capture the protruding old pine structures. Thus, the differences were relatively small in these areas. For GPNA2, the differences were consistent across the whole region. $DSM_{gen,sim}$ is slightly lower than $DSM_{gen,WV}$, and closer to reference DTM according to the values shown in the 4th column of Fig. 5c. This could be caused by the litter under the canopy or induced by the geolocation error of WorldView acquisitions. In general, differences between WorldView and simulated images exist in the open canopy, but they did not significantly influence the overall quality of each generated DSM when Bia_z and $RMSE'$ were used as the evaluation metrics. Comparing stereo surface reconstruction results from both simulated and actual images supports using DART simulations to explore the variation in spaceborne stereopair estimates of forest surfaces.

4.2. The effect of directional reflectance

As shown in Fig. 5, the characteristics of the two derived DSMs over the open forest (GPNA) can significantly differ for the two stereopairs with different acquisition geometries. This could be explained by the variation of textures induced by the directional reflectance of the canopy surfaces, which increased the complexity of matching.

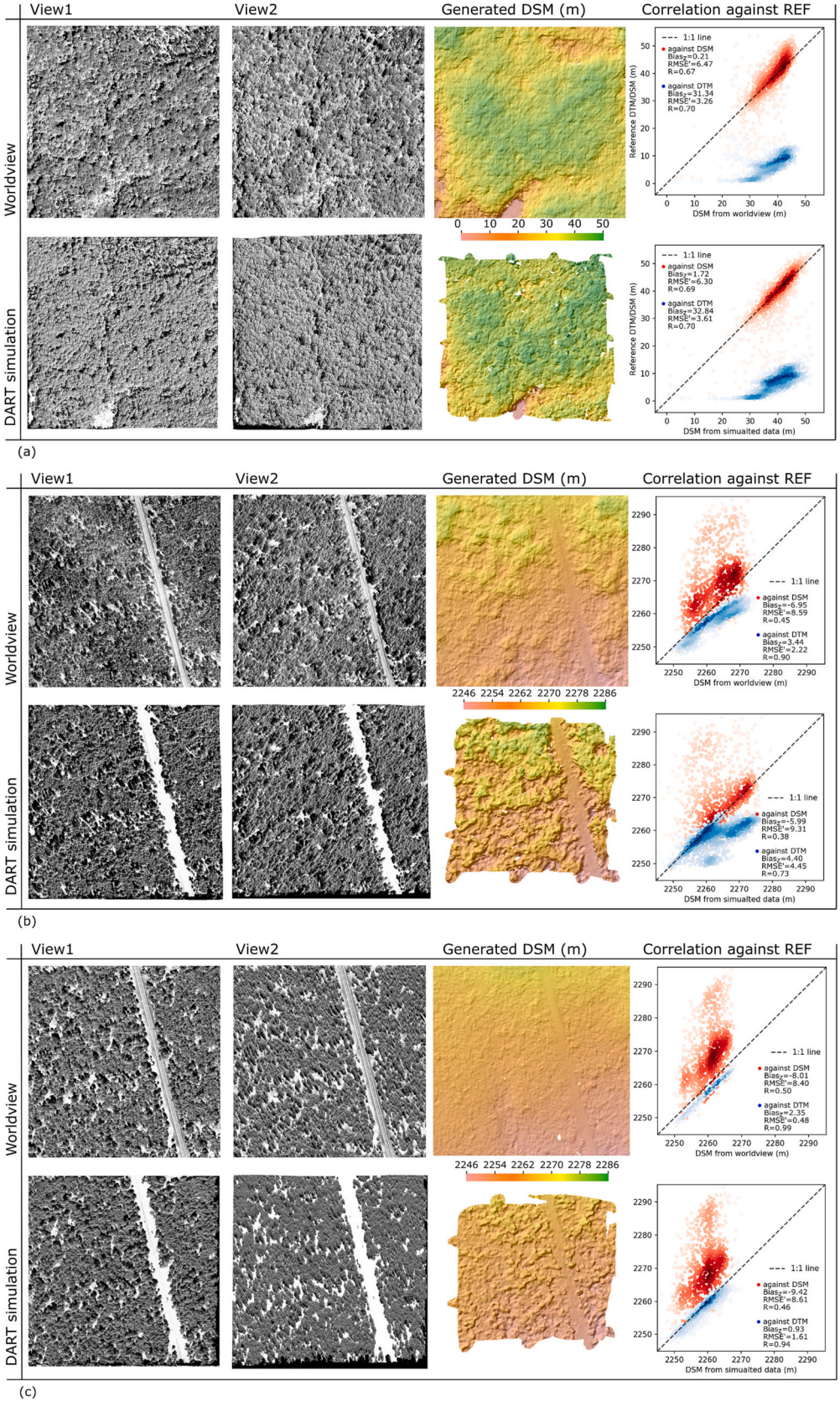

Fig. 5. Comparisons between WorldView and DART simulated top-of-atmosphere reflectance images and their derived DSMs for the three stereopairs, including (a) SERC, (b) GPNA1, and (c) GPNA2 (information shown in Table 1). Each subfigure is presented in a table format with two rows of 1) WorldView and 2) simulated data, and four columns of 1) View1 image, 2) View2 image, 3) DSM derived from the stereopair using the same colormap as DTM_{ref} and DSM_{ref} in Figs. 2, 4) correlation against DTM_{ref} (blue points) and DSM_{ref} (red points) with computed $Bias_z$, $RMSE$, and R. (For interpretation of the references to colour in this figure legend, the reader is referred to the web version of this article.)

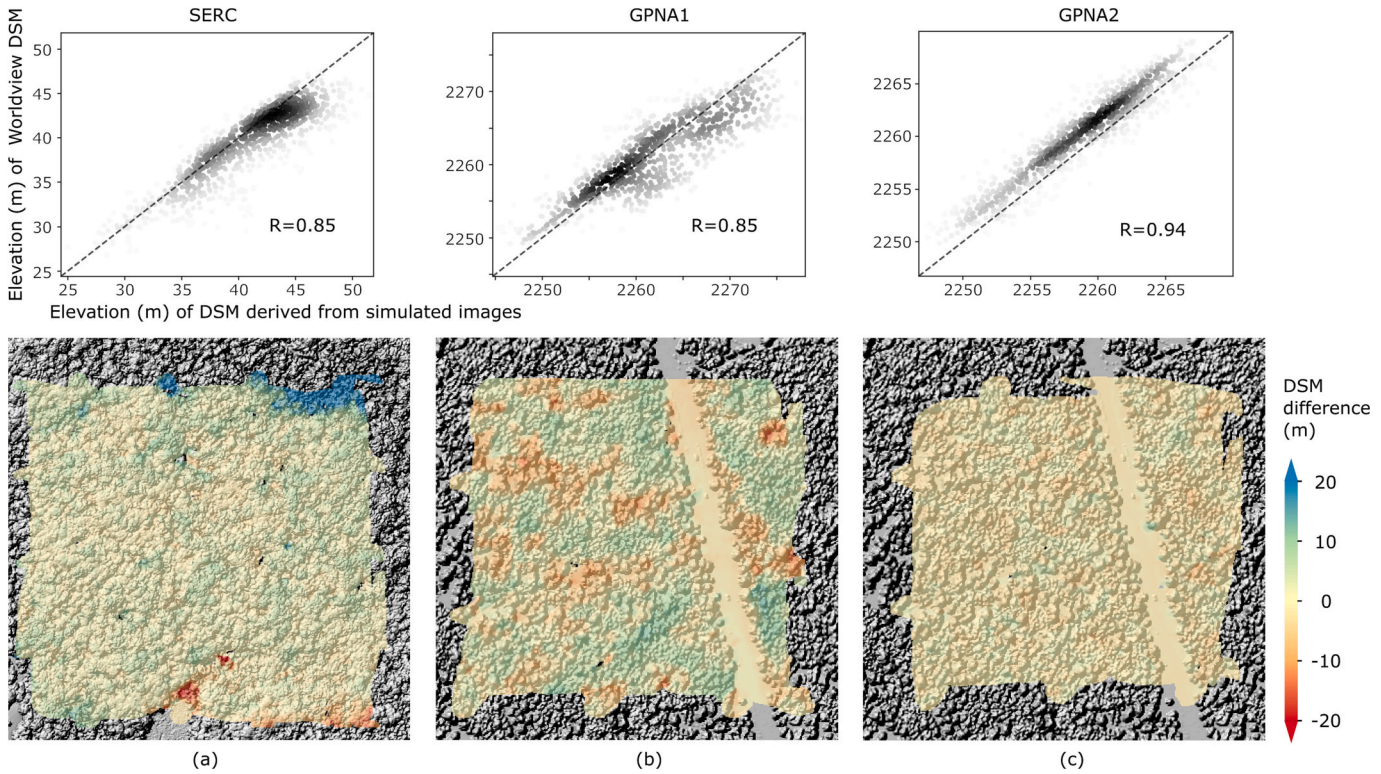

Fig. 6. Correlations (upper row, $DSM_{gen,WV}$ against $DSM_{gen,sim}$) and difference maps (lower row, $DSM_{gen,sim}$ - $DSM_{gen,WV}$) between DSMs generated from WorldView and from simulated stereopairs for (a) SERC (closed canopy); (b) GPNA1, and (c) GPNA2 (open canopy). The DSMs are shown in the 3rd column of Fig. 5.

Considering the whole scene's reflection properties, the BRF distributions at the TOA for the three stereopairs over GPNA1 and GPNA2 are shown in Fig. 7, with View1 and View2 (information in Table 1) marked with their directional reflectance (ρ) and percentage difference computed as $\frac{\rho_{view2}-\rho_{view1}}{\rho_{view1}} \times 100\%$. Because the ground was simulated as a Lambertian surface, the BRF difference mainly originated from the structural and biophysical properties of the forest. The BRF differences can be large with more complex texture correspondence from not only the canopy surface, but also the shadows and terrain features. For GPNA2, View2 was within the range influenced by the hotspot effect, so the BRF difference between the two views can reach 19.4%, compared to the smaller 12.3% difference of GPNA1.

Aside from scene-level BRF, image texture from pixel-level reflectance variation contributes significantly to feature matching and stereo image correlation success. We located the corresponding pixels of simulated images based on an implementation to generate ideal orthorectification. As illustrated in Fig. 8, the computed pixel reflectance acquired by a sensor plane is back-projected onto the surface of the DART scene following the acquisition geometry. The occluded region of the sensor's view has no reflectance value. Hence, the reflectance is vertically projected onto a horizontal plane to generate an ideal orthorectified image. The ideal orthorectifications of the simulated images using the same scene in DART are unbiased regarding the scene element positions, since the images were simulated using the same ray tracing geometry. Therefore, this method could precisely match the corresponding pixels from the two images of a stereopair. The first two

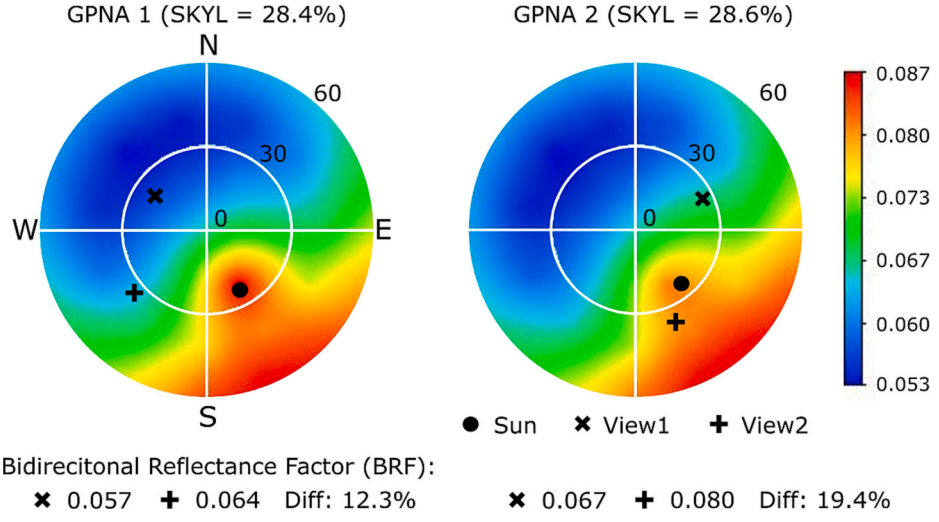

Fig. 7. Polar plots (Zenith: 0° – 60°, Azimuth: 0° – 360°) of DART-simulated BRF distribution for the two stereopairs over GPNA.

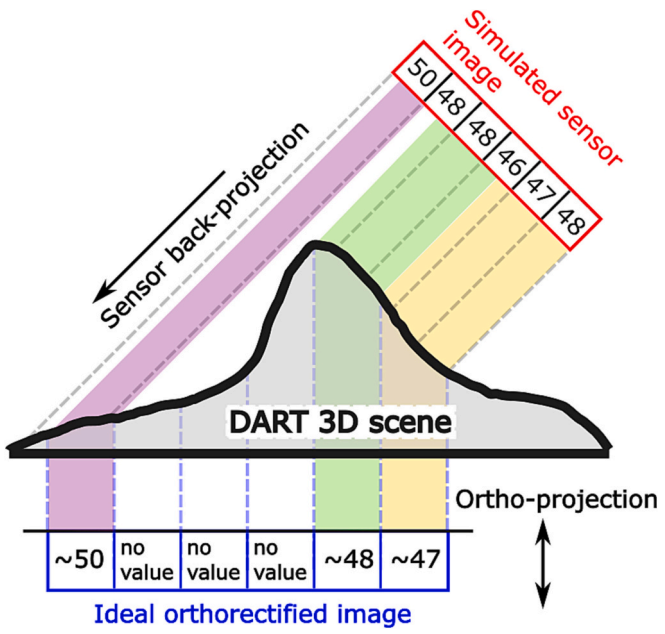

Fig. 8. Diagram for generating an ideally orthorectified image on a horizontal image plane from a sensor image in DART—modified from "industrial standard" orthorectification in DART (2023). Reflectance was computed using an area-weighted average when projecting multiple pixels from the sensor image to the horizontal image plane.

columns of Fig. 9 show the orthorectified TOA reflectance images of View1 and View2 for GPNA1 and GPNA2, where the blank pixels (no value) are regions occluded by tree crows from the view directions. After locating the matching pixels of the two ideally orthorectified images, the 3rd column shows the scattered point density distribution by correlating these pixels. The dense points in the plots' top-right corner corresponded to the directly irradiated ground pixels without shadow, which showed an apparent correlation. In contrast, the correlations of the other pixels (crowns and shadows) cannot be visually identified, especially for GPNA2. We calculated the correlation coefficient (R) of the matched pixels, which reflected the difficulty of identifying textures between two view directions. An apparent drop of R from 0.34 (GPNA1) to 0.26 (GPNA2) was observed, indicating that the hotspot effect reduced the matched textures from the tree crown, and most of the canopy features were missed in the generated DSM, thus the result is closer to DTM_{ref}.

5. Discussions and conclusions

To examine estimates of forest canopy surfaces from spaceborne stereogrammetry, we developed a VHR stereopair image simulation method using the DART 3-D radiative transfer model and evaluated the quality of the DSMs built from these simulated stereopairs against those generated from real VHR spaceborne stereopairs. Throughout the process, actual data from different sources were used for scene construction (G-LiHT point cloud), references dataset preparation (DSM and DTM derived from G-LiHT), and comparison and evaluation of results (simulated and WorldView along-track stereopairs). Two sites of closed (SERC) and open (GPNA) canopies were evaluated using three independent stereopairs. The DSMs derived from WorldView and simulated stereopairs generated promising results of comparisons. The difference

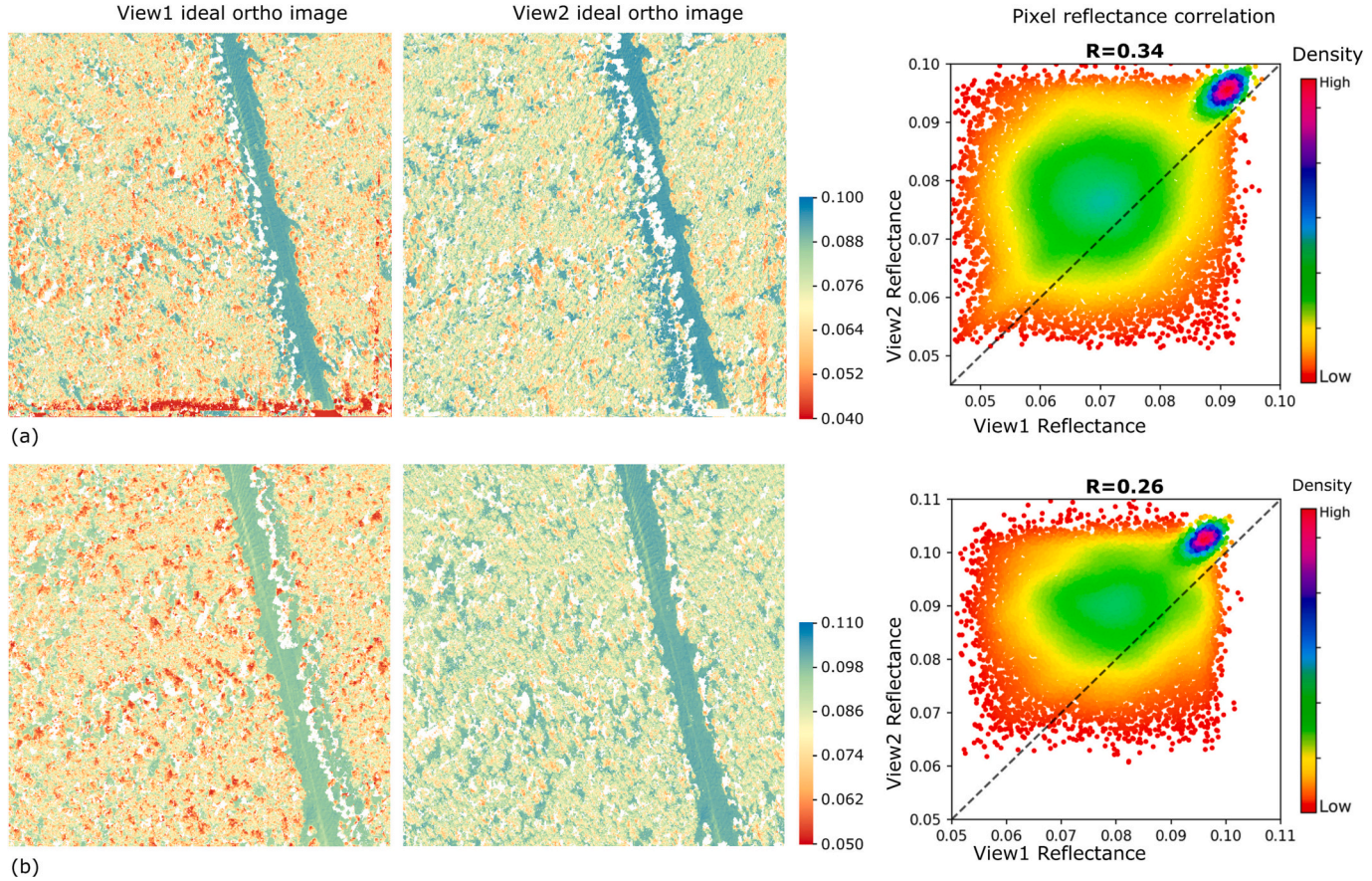

Fig. 9. Pixel reflectance correlation (right column) produced by the two ideal orthorectified DART simulated images of TOA reflectance (left column for View1 and center column for View2) for (a) GPNA1 and (b) GPNA2. The images before orthorectification are shown in Fig. 5.

in $Bias_z$ was <1.6 m; the difference in accuracy was <1 m; and the difference in R was <0.07. These results built a pathway in providing realistic simulations for various interdisciplinary post-processing research domains (e.g., image processing or computer vision). The simulation methodology is easily replicable to evaluate stereo-derived surfaces across a range of vegetation types at study sites that coincide with airborne lidar data and stereo satellite coverage.

5.1. Factors influencing generated DSM accuracy

The sun-sensor geometry and forest type can strongly influence the characteristics of the DSMs from stereogrammetry for complex forest vegetation. In this study, the WorldView stereopairs illustrated the importance of image acquisition conditions for stereogrammetry over forests. The three stereopairs of both Worldview and simulations demonstrate the resulting variation in surface estimates, which range from surfaces from the terrain (DTM_{ref}) up to the reference canopy (DSM_{ref}). The dense canopy site (SERC), where the 20—100 percentile of the canopy height is above 25 m, was the only case for which the generated DSMs were close to DSM_{ref}. For the open canopy site, GPNA1 featured the acquisition configurations typical of stereo data in existing commercial archives (~ 35° convergence angle). From this acquisition, most of the protruding crown structures of the old pines (80—100 percentile of canopy height) were missed. With the more challenging GPNA2 configuration, almost all crown textures were not identified, because the hotspot effect induced a lower pixel reflectance correlation between the two views. The overall accuracy ($RMSE^{'}$) of the generated DSM for the dense canopy (~6 m) was slightly better than that for the open canopy (~8 m).

From past studies, the accuracy of the reconstructed forest canopy can be improved by using different configurations, such as a more oblique solar zenith angle as reported by (Montesano et al., 2017, 2019), or a smaller convergence angle as reported by (Piermattei et al., 2018). The generic configurations designed for global surface elevation retrieval (e.g., ~ 35° convergence angle) could be further optimized for forests in the design of a future satellite mission (NASA, 2021). The methods developed in this study are suitable for this purpose. The current work focuses on the method for building realistic stereo data that are comparable to actual acquisitions. Based on this work, we also investigated the sensitivity of the influencing configurations of along-track VHR stereo to achieve optimization in forest surface elevation retrieval in a companion paper, using the same realistic scenes and references over dense canopies (SERC) and open forests (GPNA) (Yin et al., 2023).

5.2. Using RTMs for image simulation and post-processing applications

Traditionally, RTM was extensively applied for passive remote sensing to simulate BRF over realistic or simplified scenes for interpreting satellite acquisitions with moderate resolution (100 s of meters to kilometers). Although several 3-D RTMs are capable of forward image simulations with high resolution over heterogeneous landscapes, it was unclear whether the simulated images can be broadly used to study the post-processing application of VHR images. In this study, we demonstrated for the first time that realistic 3-D RTM simulations could be georeferenced with camera models for stereo DSM generation from simulated stereopairs. Such applications are based on image texture variation derived from complex 3-D scenes. Therefore, only 3-D RTMs are suitable for these studies.

5.3. Prospects: An evaluation tool to investigate optimal configurations and algorithms for VHR satellite missions

The developed simulation method can serve as a prototype for an in-depth study to optimize future VHR satellite configurations and algorithms to retrieve DSM and DTM with different vegetation structures and fractional covers based on realistic scenes created for forest research sites, such as NEON (Elmendorf et al., 2016). Further development of DART will incorporate spectral variability influence of narrower bands ranging from visible to near-infrared in stereo capacity, such as by simulating the acquisition of the CO3D Earth Observation program (Lebègue et al., 2020; Michel et al., 2020; Youssefi et al., 2020). In addition, tree delineation and species classification can further enhance scene construction using various physiological parameterizations.

In the current study, the PVlad model played an essential role in constructing realistic scenes of 3-D plant area density distribution from dense, multi-path G-LiHT lidar data, with georeferencing of the DART local coordinate system. >860 G-LiHT campaigns have been conducted in the USA, providing a broad range of multi-path campaigns that would be suitable for generating realistic scenes for future studies of VHR stereogrammetry. The advantages of using realistic scenes are apparent in three aspects: 1) a broad range of validation data from actual remote sensing measurements; 2) extensive field and tower-based measurements to parameterized scenes from forest research sites, such as SERC, which has a ForestGeo site (Anderson-Teixeira et al., 2015), a NEON tower, and continuous litter-collection LAI measurements; and 3) building high-fidelity realistic training data for deep learning approaches for remote sensing data interpretation.

Simulated georeferenced images with a camera model in a generic format propose a departure to unlock the current limitations of applications using 3-D RTMs. In addition to the VHR imagery simulation over a relatively small region, the application can be extended to airborne imagery simulations with a much wider field of view and a complex camera model over the selected study sites. Simulated images in GeoTIFF format can be used as inputs for most remote sensing software for a broad range of post-processing studies.

Model availability

The functionalities used in this work have been implemented in the latest release of the DART model. DART provides free licenses for research and education purposes (https://dart.omp.eu/).

Open access to the simulated data

For both SERC and GPNA, the simulated VHR images with RPC stored in GeoTIFF format and the reference DSM/DTM used in this study can be openly accessed from https://glihtdata.gsfc.nasa.gov/files/tmp/StereoModeling/.

CRediT authorship contribution statement

Tiangang Yin: Conceptualization, Methodology, Software, Writing – original draft, Investigation, Validation, Writing – review & editing. **Paul M. Montesano:** Methodology, Software, Writing – original draft, Investigation, Data curation. **Bruce D. Cook:** Data curation, Investigation, Methodology, Supervision, Writing – review & editing. **Eric Chavanon:** Methodology, Software, Visualization, Validation. **Christopher S.R. Neigh:** Conceptualization, Methodology, Software, Supervision, Writing – review & editing. **David Shean:** Conceptualization, Methodology, Software, Writing – review & editing. **Dongju Peng:** Methodology, Software, Investigation. **Nicolas Lauret:** Methodology, Software, Investigation. **Ameni Mkaouar:** Investigation, Validation, Writing – review & editing. **Douglas C. Morton:** Conceptualization, Investigation, Supervision, Writing – original draft, Writing – review & editing. **Omar Regaieg:** Methodology, Investigation, Validation. **Zhijun Zhen:** Methodology, Investigation, Validation. **Jean-Philippe Gastellu-Etchegorry:** Conceptualization, Software, Investigation, Supervision.

Declaration of Competing Interest

The authors declare that they have no known competing financial interests or personal relationships that could have appeared to influence the work reported in this paper.

Acknowledgments

This research was supported by (1) NASA Goddard Space Flight Center's Internal Research and Development Program, (2) NASA's Commercial SmallSat Data Acquisition Program (CDSA) augmentation to the Terrestrial Ecology Program [grant number NNH16ZDA001N-CARBON], and (3) NASA's Earth Science Technology Office [grant number NNH21ZDA001N-DSI]. Maxar data were provided by NASA's Commercial Archive Data for NASA investigators under the National Geospatial-Intelligence Agency's NextView license agreement. The authors are also thankful to Guoqing Sun at the University of Maryland, Rongjun Qin at Ohio State University, and Oleg Alexandrov at NASA Ames Research Center for their valuable suggestions. The authors also thank the anonymous reviewers for their valuable suggestions.

References

Aber, J.D., Reich, P.B., Goulden, M.L., 1996. Extrapolating leaf CO2 exchange to the canopy: a generalized model of forest photosynthesis compared with measurements by eddy correlation. Oecologia 106, 257–265.
Abrams, M., Crippen, R., Fujisada, H., 2020. ASTER global digital elevation model (GDEM) and ASTER global water body dataset (ASTWBD). Remote Sens. 12.
Anderson-Teixeira, K.J., Davies, S.J., Bennett, A.C., Gonzalez-Akre, E.B., Muller-Landau, H.C., Joseph Wright, S., Abu Salim, K., Almeyda Zambrano, A.M., Alonso, A., Baltzer, J.L., Basset, Y., Bourg, N.A., Broadbent, E.N., Brockelman, W.Y., Bunyavejchewin, S., Burslem, D.F.R.P., Butt, N., Cao, M., Cardenas, D., Chuyong, G. B., Clay, K., Cordell, S., Dattaraja, H.S., Deng, X., Detto, M., Du, X., Duque, A., Erikson, D.L., Ewango, C.E.N., Fischer, G.A., Fletcher, C., Foster, R.B., Giardina, C.P., Gilbert, G.S., Gunatilleke, N., Gunatilleke, S., Hao, Z., Hargrove, W.W., Hart, T.B., Hau, B.C.H., He, F., Hoffman, F.M., Howe, R.W., Hubbell, S.P., Inman-Narahari, F. M., Jansen, P.A., Jiang, M., Johnson, D.J., Kanzaki, M., Kassim, A.R., Kenfack, D., Kibet, S., Kinnaird, M.F., Korte, L., Kral, K., Kumar, J., Larson, A.J., Li, Y., Li, X., Liu, S., Lum, S.K.Y., Lutz, J.A., Ma, K., Maddalena, D.M., Makana, J.-R., Malhi, Y., Marthews, T., Mat Serudin, R., McMahon, S.M., McShea, W.J., Memiaghe, H.R., Mi, X., Mizuno, T., Morecroft, M., Myers, J.A., Novotny, V., de Oliveira, A.A., Ong, P. S., Orwig, D.A., Ostertag, R., den Ouden, J., Parker, G.G., Phillips, R.P., Sack, L., Sainge, M.N., Sang, W., Sri-ngernyuang, K., Sukumar, R., Sun, I.-F., Sungpalee, W., Suresh, H.S., Tan, S., Thomas, S.C., Thomas, D.W., Thompson, J., Turner, B.L., Uriarte, M., Valencia, R., Vallejo, M.I., Vicentini, A., Vrška, T., Wang, X., Wang, X., Weiblen, G., Wolf, A., Xu, H., Yap, S., Zimmerman, J., 2015. CTFS-ForestGEO: a worldwide network monitoring forests in an era of global change. Glob. Chang. Biol. 21, 528–549.
Antonarakis, A.S., Munger, J.W., Moorcroft, P.R., 2014. Imaging spectroscopy- and lidar-derived estimates of canopy composition and structure to improve predictions of forest carbon fluxes and ecosystem dynamics. Geophys. Res. Lett. 41, 2535–2542.
Asner, G.P., Keller, M., Silva, J.N.M., 2004. Spatial and temporal dynamics of forest canopy gaps following selective logging in the eastern Amazon. Glob. Chang. Biol. 10, 765–783.
Béland, M., Baldocchi, D.D., 2021. Vertical structure heterogeneity in broadleaf forests: effects on light interception and canopy photosynthesis. Agric. For. Meteorol. 307, 108525.
Berk, A., Bernstein, L.S., Robertson, D.C., 1987. MODTRAN: a moderate resolution model for LOWTRAN. Spectral Sciences Inc, Burlington MA.
Beyer, R.A., Alexandrov, O., McMichael, S., 2018. The Ames stereo pipeline: NASA's open source software for deriving and processing terrain data. Earth Space Sci. 5, 537–548.
Chai, J.-X., Shum, H.-Y., 2000. Parallel projections for stereo reconstruction. In: Proceedings IEEE Conference on Computer Vision and Pattern Recognition. CVPR 2000 (Cat. No.PR00662, vol.492, pp. 493–500.
Cook, B., Corp, L., Nelson, R., Middleton, E., Morton, D., McCorkel, J., Masek, J., Ranson, K., Ly, V., Montesano, P., 2013. NASA Goddard's LiDAR, hyperspectral and thermal (G-LiHT) airborne imager. Remote Sens. 5, 4045.
d'Angelo, P., Reinartz, P., 2012. Semiglobal matching results on the isprs stereo matching benchmarK. Int. Arch. Photogramm. Remote Sens. Spatial Inf. Sci. XXXVIII-4/W19, 79–84.
d'Oliveira, M.V.N., Figueiredo, E.O., de Almeida, D.R.A., Oliveira, L.C., Silva, C.A., Nelson, B.W., da Cunha, R.M., de Almeida Papa, D., Stark, S.C., Valbuena, R., 2021. Impacts of selective logging on Amazon forest canopy structure and biomass with a LiDAR and photogrammetric survey sequence. For. Ecol. Manag. 500, 119648.
DART, 2023. DART User Manual.
Disney, M., Lewis, P., North, P., 2000. Monte Carlo ray tracing in optical canopy reflectance modelling. Remote Sens. Rev. 18, 163–196.
Dissegna, M.A., Yin, T., Wei, S., Richards, D., Grêt-Regamey, A., 2019. 3-D reconstruction of an urban landscape to assess the influence of vegetation in the radiative budget. Forests 10, 700.
Duncanson, L., Rourke, O., Dubayah, R., 2015. Small sample sizes yield biased allometric equations in temperate forests. Sci. Rep. 5, 17153.
Elmendorf, S.C., Jones, K.D., Cook, B.I., Diez, J.M., Enquist, C.A.F., Hufft, R.A., Jones, M. O., Mazer, S.J., Miller-Rushing, A.J., Moore, D.J.P., Schwartz, M.D., Weltzin, J.F., 2016. The plant phenology monitoring design for the National Ecological Observatory Network. Ecosphere 7, e01303.
Feng, Y., Negrón-Juárez, R.I., Chambers, J.Q., 2020. Remote sensing and statistical analysis of the effects of hurricane María on the forests of Puerto Rico. Remote Sens. Environ. 247, 111940.
Flathers, K.N., Kolb, T.E., Bradford, J.B., Waring, K.M., Moser, W.K., 2016. Long-term thinning alters ponderosa pine reproduction in northern Arizona. For. Ecol. Manag. 374, 154–165.
Fletcher, R., 1971. A modified Marquardt subroutine for non-linear least squares.
Fraser, C.S., Hanley, H.B., 2003. Bias compensation in rational functions for IKONOS satellite imagery. Photogramm. Eng. Remote Sens. 69, 53–57.
Gastellu-Etchegorry, J.-P., Demarez, V., Pinel, V., Zagolski, F., 1996. Modeling radiative transfer in heterogeneous 3-d vegetation canopies. Remote Sens. Environ. 58, 131–156.
Gastellu-Etchegorry, J.-P., Yin, T., Lauret, N., Cajgfinger, T., Gregoire, T., Grau, E., Feret, J.-B., Lopes, M., Guilleux, J., Dedieu, G., Malenovský, Z., Cook, B., Morton, D., Rubio, J., Durrieu, S., Cazanave, G., Martin, E., Ristorcelli, T., 2015. Discrete anisotropic radiative transfer (DART 5) for modeling airborne and satellite spectroradiometer and LIDAR acquisitions of natural and urban landscapes. Remote Sens. 7, 1667–1701.
Gastellu-Etchegorry, J.P., Lauret, N., Yin, T., Landier, L., Kallel, A., Malenovský, Z., Bitar, A.A., Aval, J., Benhmida, S., Qi, J., Medjdoub, G., Guilleux, J., Chavanon, E., Cook, B., Morton, D., Chrysoulakis, N., Mitraka, Z., 2017. DART: recent advances in remote sensing data modeling with atmosphere, polarization, and chlorophyll fluorescence. IEEE J. Select. Top. Appl. Earth Observ. Remote Sens. 10, 2640–2649.
Goodenough, A., Brown, S., 2012. DIRSIG 5: core design and implementation. SPIE.
Govaerts, Y.M., Verstraete, M.M., 1998. Raytran: a Monte Carlo ray-tracing model to compute light scattering in three-dimensional heterogeneous media. IEEE Trans. Geosci. Remote Sens. 36, 493–505.
Grau, E., Gastellu-Etchegorry, J.-P., 2013. Radiative transfer modeling in the earth-atmosphere system with DART model. Remote Sens. Environ. 139, 149–170.
Gupta, R., Hartley, R.I., 1997. Linear pushbroom cameras. IEEE Trans. Pattern Anal. Mach. Intell. 19, 963–975.
Hirschmuller, H., 2008. Stereo processing by semiglobal matching and mutual information. IEEE Trans. Pattern Anal. Mach. Intell. 30, 328–341.
Howat, I.M., Porter, C., Smith, B.E., Noh, M.J., Morin, P., 2019. The reference elevation model of Antarctica. Cryosphere 13, 665–674.
Hu, H., Chen, C., Wu, B., Yang, X., Zhu, Q., Ding, Y., 2016. Texture-aware dense image matching using ternary census transform. In: ISPRS annals of the photogrammetry, remote sensing and spatial information sciences, XXIII ISPRS Congress. Prague, Czech Republic.
Jones, H.G., Vaughan, R.A., 2010. Remote sensing of vegetation: principles, techniques, and applications. Oxford University Press.
Kamoske, A.G., Dahlin, K.M., Stark, S.C., Serbin, S.P., 2019. Leaf area density from airborne LiDAR: comparing sensors and resolutions in a temperate broadleaf forest ecosystem. For. Ecol. Manag. 433, 364–375.
Kampe, T., Johnson, B., Kuester, M., Keller, M., 2010. NEON: the first continental-scale ecological observatory with airborne remote sensing of vegetation canopy biochemistry and structure. J. Appl. Remote. Sens. 4, 043510.
Kobayashi, H., Iwabuchi, H., 2008. A coupled 1-D atmosphere and 3-D canopy radiative transfer model for canopy reflectance, light environment, and photosynthesis simulation in a heterogeneous landscape. Remote Sens. Environ. 112, 173–185.
Kükenbrink, D., Schneider, F.D., Schmid, B., Gastellu-Etchegorry, J.-P., Schaepman, M. E., Morsdorf, F., 2021. Modelling of three-dimensional, diurnal light extinction in two contrasting forests. Agric. For. Meteorol. 296, 108230.
Lebègue, L., Cazala-Hourcade, E., Languille, F., Artigues, S., Melet, O., 2020. CO3D, a worldwide one one-meter accuracy dem for 2025. The International Archives of Photogrammetry, Remote Sensing and Spatial Information Sciences 43, 299–304.
Lemoine, F.G., Kenyon, S.C., Factor, J.K., Trimmer, R.G., Pavlis, N.K., Chinn, D.S., Cox, C.M., Klosko, S.M., Luthcke, S.B., Torrence, M.H., 1998. The development of the joint NASA GSFC and the National Imagery and Mapping Agency (NIMA) geopotential model EGM96. In.
Lesiv, M., See, L., Laso Bayas, J.C., Sturn, T., Schepaschenko, D., Karner, M., Moorthy, I., McCallum, I., Fritz, S., 2018. Characterizing the spatial and temporal availability of very high resolution satellite imagery in Google earth and Microsoft bing maps as a source of reference data. Land 7, 118.
Michel, J., Sarrazin, E., Youssefi, D., Cournet, M., Buffe, F., Delvit, J., Emilien, A., Bosman, J., Melet, O., L'Helguen, C., 2020. A new satellite imagery stereo pipeline designed for scalability, robustness and performance. ISPRS Ann. Photogramm. Remote Sens. Spat. Inform. Sci. 2, 171–178.
Mitchard, E.T.A., 2018. The tropical forest carbon cycle and climate change. Nature 559, 527–534.
Montesano, P.M., Neigh, C., Sun, G., Duncanson, L., Van Den Hoek, J., Ranson, K.J., 2017. The use of sun elevation angle for stereogrammetric boreal forest height in open canopies. Remote Sens. Environ. 196, 76–88.
Montesano, P.M., Neigh, C.S.R., Wagner, W., Wooten, M., Cook, B.D., 2019. Boreal canopy surfaces from spaceborne stereogrammetry. Remote Sens. Environ. 225, 148–159.

Moratto, Z.M., Broxton, M.J., Beyer, R.A., Lundy, M., Husmann, K., 2010. Ames Stereo Pipeline, NASA's open source automated stereogrammetry software. In: Lunar and Planetary Science Conference, p. 2364.
Moré, J.J., 1978. In: The Levenberg-Marquardt Algorithm: Implementation and Theory. Springer Berlin Heidelberg, Berlin, Heidelberg, pp. 105–116.
Morrison, W., Yin, T., Lauret, N., Guilleux, J., Kotthaus, S., Gastellu-Etchegorry, J.-P., Norford, L., Grimmond, S., 2020. Atmospheric and emissivity corrections for ground-based thermography using 3D radiative transfer modelling. Remote Sens. Environ. 237, 111524.
Myneni, R.B., Asrar, G., Hall, F.G., 1992. A three-dimensional radiative transfer method for optical remote sensing of vegetated land surfaces. Remote Sens. Environ. 41, 105–121.
Myneni, R.B., Ross, J., 2012. Photon-Vegetation Interactions: Applications in Optical Remote Sensing and Plant Ecology. Springer Science & Business Media.
NASA, 2021. Observing Earth's changing surface topography and vegetation structure – A frame work for the decade, NASA's surface topography and vegetation incubation study white paper. . In.
Nefian, A.V., Husmann, K., Broxton, M., Lundy, M., Hancher, M.D., To, 2009. A bayesian formulation for sub-pixel refinement in stereo orbital imagery. In: 2009 16th IEEE International Conference on Image Processing (ICIP), pp. 2361–2364.
Neigh, C.S.R., Masek, J.G., Bourget, P., Cook, B., Huang, C., Rishmawi, K., Zhao, F., 2014. Deciphering the precision of stereo IKONOS canopy height models for US forests with G-LiHT airborne LiDAR. Remote Sens. 6, 1762–1782.
Neigh, C.S.R., Masek, J.G., Bourget, P., Rishmawi, K., Zhao, F., Huang, C., Cook, B.D., Nelson, R.F., 2016. Regional rates of young US forest growth estimated from annual landsat disturbance history and IKONOS stereo imagery. Remote Sens. Environ. 173, 282–293.
Neigh, C.S.R., Masek, J.G., Nickeson, J.E., 2013. High-resolution satellite data open for government research. Eos, Trans. Am. Geophys. Union 94, 121–123.
Ni, W., Sun, G., Ranson, K.J., Montesano, P., Liu, Q., Li, Z., Kharuk, V.I., Zhang, Z., 2019. LandRS: a Virtual Constellation Simulator for InSAR, LiDAR Waveform and Stereo Imagery Over Mountainous Forest Landscapes. In: IGARSS 2019 - 2019 IEEE International Geoscience and Remote Sensing Symposium, pp. 4892–4895.
Ni, W., Zhang, Z., Sun, G., Liu, Q., 2019b. Modeling the stereoscopic features of mountainous Forest landscapes for the extraction of Forest Heights from stereo imagery. Remote Sens. 11, 1222.
Noh, M.-J., Howat, I.M., 2017. The surface extraction from TIN based search-space minimization (SETSM) algorithm. ISPRS J. Photogramm. Remote Sens. 129, 55–76.
North, P., 1996. Three-dimensional forest light interaction model using a Monte Carlo method. Geosci. Remote Sens. IEEE Trans. 34 (34), 946–956.
Parker, G., Martínez-Yrízar, A., Álvarez-Yépiz, J.C., Maass, M., Araiza, S., 2018. Effects of hurricane disturbance on a tropical dry forest canopy in western Mexico. For. Ecol. Manag. 426, 39–52.
Parker, G.G., 1995. Structure and microclimate of forest canopies. Forest canopies. 73–106.
Piermattei, L., Marty, M., Karel, W., Ressl, C., Hollaus, M., Ginzler, C., Pfeifer, N., 2018. Impact of the acquisition geometry of very high-resolution Pléiades imagery on the accuracy of canopy height models over forested alpine regions. Remote Sens. 10, 1542.
Pomerleau, F., Colas, F., Siegwart, R., Magnenat, S., 2013. Comparing ICP variants on real-world data sets. Auton. Robot. 34, 133–148.
Porter, C., Morin, P., Howat, I., Noh, M.-J., Bates, B., Peterman, K., Keesey, S., Schlenk, M., Gardiner, J., Tomko, K., 2018. ArcticDEM. Harvard Dataverse, 1, 2018-2030.2008.
Qi, J., Gastellu-Etchegorry, J.P., Yin, T., 2018. Reconstruction of 3D forest mock-ups from airborne LiDAR data for multispectral image simulation using DART model. In: IGARSS 2018 - 2018 IEEE International Geoscience and Remote Sensing Symposium, pp. 3975–3978.
Qi, J., Xie, D., Yin, T., Yan, G., Gastellu-Etchegorry, J.-P., Li, L., Zhang, W., Mu, X., Norford, L.K., 2019. LESS: LargE-scale remote sensing data and image simulation framework over heterogeneous 3D scenes. Remote Sens. Environ. 221, 695–706.
Qin, R., 2014. Change detection on LOD 2 building models with very high resolution spaceborne stereo imagery. ISPRS J. Photogramm. Remote Sens. 96, 179–192.
Qin, R., 2019. A critical analysis of satellite stereo pairs for digital surface model generation and a matching quality prediction model. ISPRS J. Photogramm. Remote Sens. 154, 139–150.
Regaieg, O., Yin, T., Malenovský, Z., Cook, B.D., Morton, D.C., Gastellu-Etchegorry, J.-P., 2021. Assessing impacts of canopy 3D structure on chlorophyll fluorescence radiance and radiative budget of deciduous forest stands using DART. Remote Sens. Environ. 265, 112673.
Rothermel, M., Wenzel, K., Fritsch, D., Haala, N., 2012. SURE: Photogrammetric surface reconstruction from imagery. In: Proceedings LC3D Workshop, Berlin.
Roujean, J.-L., Leroy, M., Deschamps, P.-Y., 1992. A bidirectional reflectance model of the Earth's surface for the correction of remote sensing data. J. Geophys. Res. Atmos. 97, 20455–20468.
Schaepman-Strub, G., Schaepman, M.E., Painter, T.H., Dangel, S., Martonchik, J.V., 2006. Reflectance quantities in optical remote sensing—definitions and case studies. Remote Sens. Environ. 103, 27–42.
Schneider, F.D., Leiterer, R., Morsdorf, F., Gastellu-Etchegorry, J.-P., Lauret, N., Pfeifer, N., Schaepman, M.E., 2014a. Simulating imaging spectrometer data: 3D forest modeling based on LiDAR and in situ data. Remote Sens. Environ. 152, 235–250.
Schneider, F.D., Yin, T., Gastellu-Etchegorry, J., Morsdorf, F., Schaepman, M.E., 2014. At-sensor radiance simulation for airborne imaging spectroscopy. In: 2014 6th Workshop on Hyperspectral Image and Signal Processing: Evolution in Remote Sensing (WHISPERS), pp. 1–4.
Shean, D.E., Alexandrov, O., Moratto, Z.M., Smith, B.E., Joughin, I.R., Porter, C., Morin, P., 2016. An automated, open-source pipeline for mass production of digital elevation models (DEMs) from very-high-resolution commercial stereo satellite imagery. ISPRS J. Photogramm. Remote Sens. 116, 101–117.
Shean, D.E., Bhushan, S., Montesano, P., Rounce, D.R., Arendt, A., Osmanoglu, B., 2020. A systematic, regional assessment of High Mountain Asia glacier mass balance. Front.Earth Sci. 7.
Shi, B., Wu, Z., Mo, Z., Duan, D., Yeung, S.-K., Tan, P., 2016. A benchmark dataset and evaluation for non-lambertian and uncalibrated photometric stereo. In: Proceedings of the IEEE Conference on Computer Vision and Pattern Recognition, pp. 3707–3716.
Sonka, M., Hlavac, V., Boyle, R., 2014. Image processing, analysis, and machine vision. Cengage Learning.
St-Onge, B., Hu, Y., Vega, C., 2008. Mapping the height and above-ground biomass of a mixed forest using lidar and stereo ikonos images. Int. J. Remote Sens. 29, 1277–1294.
Sun, J., Smith, M., Smith, L., Midha, S., Bamber, J., 2007. Object surface recovery using a multi-light photometric stereo technique for non-lambertian surfaces subject to shadows and specularities. Image Vis. Comput. 25, 1050–1057.
Tack, F., Buyuksalih, G., Goossens, R., 2012. 3D building reconstruction based on given ground plan information and surface models extracted from spaceborne imagery. ISPRS J. Photogramm. Remote Sens. 67, 52–64.
Tadono, T., Ishida, H., Oda, F., Naito, S., Minakawa, K., Iwamoto, H., 2014. Precise global DEM generation by ALOS PRISM. ISPRS Ann. Photogramm. Remote Sens. Spat. Inform. Sci. 2, 71.
Tao, C.V., Hu, Y., 2001. A comprehensive study of the rational function model for photogrammetric processing. Photogramm. Eng. Remote. Sens. 67, 1347–1358.
Wallin, K.F., Kolb, T.E., Skov, K.R., Wagner, M.R., 2004. Seven-year results of thinning and burning restoration treatments on old ponderosa pines at the gus Pearson natural area. Restor. Ecol. 12, 239–247.
Wang, Y., Gastellu-Etchegorry, J.-P., 2021. Accurate and fast simulation of remote sensing images at top of atmosphere with DART-lux. Remote Sens. Environ. 256, 112311.
Wei, S., Yin, T., Dissegna, M.A., Whittle, A.J., Ow, G.L.F., Yusof, M.L.M., Lauret, N., Gastellu-Etchegorry, J.-P., 2020. An assessment study of three indirect methods for estimating leaf area density and leaf area index of individual trees. Agric. For. Meteorol. 292–293, 108101.
Widlowski, J.-L., Taberner, M., Pinty, B., Bruniquel-Pinel, V., Disney, M., Fernandes, R., Gastellu-Etchegorry, J.-P., Gobron, N., Kuusk, A., Lavergne, T., Leblanc, S., Lewis, P. E., Martin, E., Möttus, M., North, P.R.J., Qin, W., Robustelli, M., Rochdi, N., Ruiloba, R., Soler, C., Thompson, R., Verhoef, W., Verstraete, M.M., Xie, D., 2007. Third radiation transfer model intercomparison (RAMI) exercise: documenting progress in canopy reflectance models. J. Geophys. Res. Atmos. 112.
Wu, S., Wen, J., Gastellu-Etchegorry, J.-P., Liu, Q., You, D., Xiao, Q., Hao, D., Lin, X., Yin, T., 2019. The definition of remotely sensed reflectance quantities suitable for rugged terrain. Remote Sens. Environ. 225, 403–415.
Xiang, J., Li, Z., Blaauw, D., Kim, H.S., Chakrabarti, C., 2016. Low complexity optical flow using neighbor-guided semi-global matching. In: 2016 IEEE International Conference on Image Processing (ICIP), pp. 4483–4487.
Yin, T., Cook, B.D., Morton, D.C., 2022. Three-dimensional estimation of deciduous forest canopy structure and leaf area using multi-directional, leaf-on and leaf-off airborne lidar data. Agric. For. Meteorol. 314, 108781.
Yin, T., Gastellu-Etchegorry, J.-P., Lauret, N., Grau, E., Rubio, J., 2013. A new approach of direction discretization and oversampling for 3D anisotropic radiative transfer modeling. Remote Sens. Environ. 135, 213–223.
Yin, T., Lauret, N., Gastellu-Etchegorry, J.-P., 2015. Simulating images of passive sensors with finite field of view by coupling 3-D radiative transfer model and sensor perspective projection. Remote Sens. Environ. 162, 169–185.
Yin, T., Montesano, P.M., Cook, B.D., Neigh, C.S.R., Morton, D.C., Chavanon, E., Lauret, N., Peng, D., Regaieg, O., Gastellu-Etchegorry, J.-P., 2023. Modeling forest canopy surface retrievals using very high-resolution spaceborne stereogrammetry: (II) optimizing acquisition configurations. Remote Sensing of Environment (Under Review).
Yin, T., Qi, J., Cook, B.D., Morton, D.C., Wei, S., Gastellu-Etchegorry, J.-P., 2020. Modeling small-footprint airborne lidar-derived estimates of gap probability and leaf area index. Remote Sens. 12, 4.
Youssefi, D., Michel, J., Sarrazin, E., Buffe, F., Cournet, M., Delvit, J.M., Helguen, C.L., Melet, O., Emilien, A., Bosman, J., 2020. CARS: a photogrammetry pipeline using dask graphs to construct a global 3D model. In: IGARSS 2020 - 2020 IEEE International Geoscience and Remote Sensing Symposium, pp. 453–456.
Zhang, K., Chen, S.-C., Whitman, D., Shyu, M.-L., Yan, J., Zhang, C., 2003. A progressive morphological filter for removing nonground measurements from airborne LIDAR data. IEEE Trans. Geosci. Remote Sens. 41, 872–882.
Zhao, F., Li, Z., Verhoef, W., Fan, C., Luan, H., Yin, T., Zhang, J., Liu, Z., Tong, C., Bao, Y., 2022. Simulation of solar-induced chlorophyll fluorescence by modeling radiative coupling between vegetation and atmosphere with WPS. Remote Sens. Environ. 277, 113075.